PHYSICAL REVIEW B **91**, 245408 (2015)

Core-shell nanostructure in a $Ge_{0.9}Mn_{0.1}$ film observed via structural and magnetic measurements

P. Dalmas de Réotier,[1,2] E. Prestat,[3,4] P. Bayle-Guillemaud,[3,4] M. Boukhari,[3,4] A. Barski,[3,4] A. Marty,[3,4] M. Jamet,[3,4] A. Suter,[5]
T. Prokscha,[5] Z. Salman,[5] E. Morenzoni,[5] and A. Yaouanc[1,2]
[1]*Université Grenoble Alpes, INAC-SPSMS, F-38000 Grenoble, France*
[2]*CEA, INAC-SPSMS, F-38000 Grenoble, France*
[3]*Université Grenoble Alpes, INAC-SP2M, F-38000 Grenoble, France*
[4]*CEA, INAC-SP2M, F-38000 Grenoble, France*
[5]*Laboratory for Muon-Spin Spectroscopy, Paul Scherrer Institute, CH-5232 Villigen-PSI, Switzerland*
(Received 12 February 2015; revised manuscript received 17 April 2015; published 8 June 2015)

Manganese-doped germanium films are model systems for the study of nanospinodal decomposition into Mn-rich nanostructures and its influence on the electronic and magnetic properties. Here we study a film of $Ge_{0.9}Mn_{0.1}$ forming self-organized nanocolumns perpendicular to a Ge substrate with high resolution scanning transmission electron microscopy combined with electron energy loss spectroscopy, bulk magnetization, and muon spin rotation and relaxation (μSR) measurements. The Mn-rich nanocolumns approximately form a triangular lattice with no detectable Mn atoms in the matrix. We find that they consist of cores surrounded by shells. The combined analysis of bulk magnetization and μSR data enables us to characterize the electronic and magnetic properties of both the cores and shells. We argue that the discovered phase separation of the columns between a core and a shell is relevant for other transition-metal-doped semiconductors.

DOI: 10.1103/PhysRevB.91.245408 PACS number(s): 75.50.Pp, 75.75.Cd, 68.37.Og, 76.75.+i

I. INTRODUCTION

Spin-polarized carriers in spintronic applications may be conveyed by conventional metallic ferromagnets or by ferromagnetic semiconductors. Until now semiconductor spintronics has mainly been based on diluted magnetic semiconductors [1–6]. Another route consists of the use of films with a well-defined pattern of transition-metal-rich nanostructures with a relatively high-temperature ferromagnetic phase. Vertical elongated nanostructures like nanocolumns are one of these structures [7–9]. They have been observed by several groups in Mn-doped germanium films [10–14] as well as in Cr-doped ZnTe films [15].

The magnetic properties of these films have so far been investigated by x-ray magnetic circular dichroism [16–18] and electron spin resonance [19–21], but the most conclusive results stem from superconducting quantum interference device (SQUID) magnetometry [22–24]. Here we resolve the structure of the nanocolumns in the $Ge_{0.9}Mn_{0.1}$ film at the atomic scale using high resolution scanning transmission electron microscopy (STEM) supplemented with electron energy loss spectroscopy (EELS) analysis. We characterize their magnetism with SQUID and muon spin rotation and relaxation (μSR) measurements. The films consist of nanocolumns embedded in a Ge matrix with less than 0.05 at. % of Mn. Each nanocolumn is made of a core surrounded by a shell with notable different magnetic properties. We suggest that this threefold structural and magnetic phase separation is generic to impurity doped semiconductors with nanospinodal decomposition.

The 80-nm-thick $Ge_{0.9}Mn_{0.1}$ film was grown by molecular beam epitaxy at low temperature. Ge and Mn atoms have been co-evaporated at 100 °C on a Ge(100) substrate using standard Knudsen cells. Due to the very low solubility of Mn in Ge, a spontaneous two-dimensional spinodal decomposition takes place within the film at the early stage of the growth [25]. The subsequent layer-by-layer growth leads to the formation of Mn-rich nanocolumns spanning the whole film thickness [14]. Their average diameter is $d_{\rm nc} = 4$ nm—see the images in Appendix A. The nanocolumns approximately form a triangular lattice with an average lattice parameter $d_{\rm nc}^{\rm lp} = 10$ nm and a correlation length of a few $d_{\rm nc}^{\rm lp}$ (Appendix B).

The STEM-EELS analysis was performed at room temperature with an Å-sized electron probe. The μSR spectra were recorded from 300 down to 5 K at the low energy muon (LEM) spectrometer [26,27] of the Swiss Muon Source (SμS, Paul Scherrer Institute, Switzerland) with a 9 cm^2 area sample. The measurements were carried out either in zero or in an external field $\mathbf{B}_{\rm ext}$ applied perpendicular to the film substrate.

II. ELECTRON MICROSCOPY

Results of STEM-EELS measurements are presented in Fig. 1. The nanocolumns exhibit a rather complex inner crystal structure and are surrounded by a Ge matrix with huge tensile strain up to 1.0 (3)%. The dark ring marked by the inner orange circle in Fig. 1(b) is an interfacial region separating two phases [28]. As shown in Fig. 1(c), the Mn content within the nanocolumns is not uniform: This leads to a core-shell structure with a $d_{\rm core} = 2$ nm core diameter containing a nearly homogeneous concentration of 65 at. % of Mn surrounded with a $r_{\rm s} = 1$ nm thick shell in which the Mn content decreases roughly linearly from 65 to less than 0.05 at. %—the detection limit of atom probe tomography [29]—in the matrix. The average Mn content of 33 at. % over the total area agrees with a previous estimate [29].

The atomic density in the nanocolumn core is large: 82 (8) atoms/nm^3 to be compared to 44 atoms/nm^3 in pure Ge. A close packed metallic structure is therefore formed in the nanocolumns. It is tempting to assign it to the stable Ge-Mn alloy of formula Ge_3Mn_5 since its Mn atomic fraction of 5/8 is close to the value measured in the nanocolumns core [30]. However, x-ray diffraction has definitely excluded the

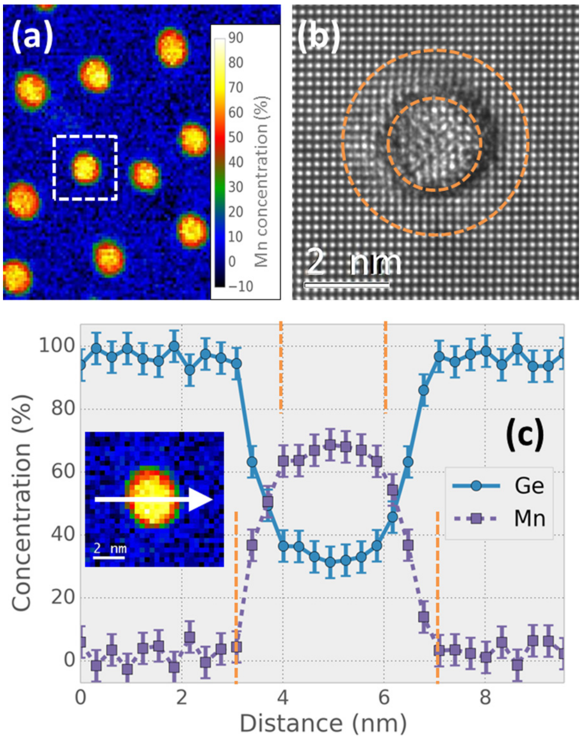

FIG. 1. (Color online) Characterization of the $Ge_{0.9}Mn_{0.1}$ film. (a) Mn concentration map obtained by EELS. (b) STEM plane view. (c) Ge and Mn concentration profiles across a single nanocolumn. In (b) and (c) the orange dashed circles and vertical dashed lines specify the nanocolumn core and shell positions.

presence of the hexagonal Ge_3Mn_5 phase within the film [31]. Magnetization measurements discussed below also support this result since the magnetic moment per Mn in the core is much less than 2.6 μ_B/Mn in pure Ge_3Mn_5. An exhaustive investigation of the possible phases concluded to an alpha type Ge_2Mn phase in the columns [28]. It consists of a simple cubic lattice of Ge atoms hosting Mn at interstitial sites located at the center of the cube. For the nominal composition Ge_2Mn every second interstitial site is occupied, but depending on the occupancy of the interstitial site the structure can accommodate large variations in the relative atomic fractions of Ge and Mn. Here, since the columns contain more Mn than Ge atoms, we conjecture that all the interstitial sites are occupied and some of the Mn atoms are in substitutional Ge sites.

Concerning the Mn atomic density, it varies from 53 (6) atoms/nm^3 in the nanocolumns core down to approximately zero in the Ge matrix. Assuming a linearly decreasing Mn concentration profile in the shell, we find that 3/7 (4/7) of Mn atoms are located in the nanocolumns core (shell).

In summary of the electron microscopy study, we find the columns to be embedded in a Ge matrix which is free of Mn and to be made of a core and a shell. Both the Mn concentration and the atomic density are large in the core. Its structure is most likely of Ge_2Mn alpha type. The Mn concentration sharply decreases in the shell which is more diamondlike. Strong strains are present at the interface between the core and the shell.

III. MAGNETIC MEASUREMENTS

A. SQUID measurements

We now present the magnetization data. From the signal obtained upon field cooling (FC) the film in 5 T down to 5 K [Fig. 2(a)] two magnetic transitions are inferred: a first one close to room temperature and a second one below 30 K. This large difference in the transition temperatures suggests that two very distinct regions in the film are involved. The Mn concentration in the matrix is too small for the matrix to be involved in any of the transitions. The two transitions could therefore concern the cores and shells inferred from microscopy. The μSR data presented below will confirm this hypothesis and allow us to assign each of the transitions with the cores and the shells. At present we give the saturation magnetization for the cores: 30 kA/m when normalized to the film volume [dashed line in Fig. 2(a)], i.e., 827 kA/m with respect to the core volume. This corresponds to a core moment of $\mu_{\mathrm{core}} = 1.7\,\mu_B$/Mn. The shell magnetization at 5 K is the difference between the low temperature magnetization of the film, i.e., 43 kA/m on average for the two field directions, and

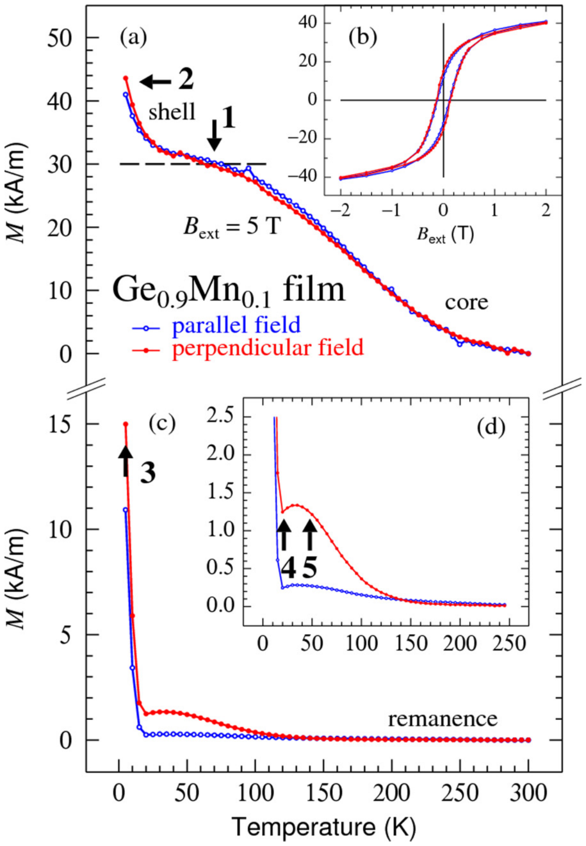

FIG. 2. (Color online) Bulk magnetization measurements for the $Ge_{0.9}Mn_{0.1}$ film normalized to its volume. The field $\mathbf{B}_{\mathrm{ext}}$ is either parallel or perpendicular to the film substrate. (a) Magnetization vs temperature while cooling the film under 5 T. (b) Magnetization cycles recorded at 5 K. (c) Remanent magnetization as a function of temperature obtained after field cooling under 5 T down to 5 K and switching off the field. For the sake of clarity the magnetization between 10 and 250 K has been enlarged in (d). The different magnetic configurations denoted 1 to 5 are discussed in the text and illustrated in Fig. 5.

the core contribution. It is $\simeq 13$ kA/m [Fig. 2(a)]. Interestingly this value of 13 kA/m corresponds to the average of the remanence signals at 5 K for the two field directions [Fig. 2(c)]. Scaled to the shell volume this magnetization amounts to 124 kA/m, i.e., an average moment $\mu_{\mathrm{shell}} = 0.6\,\mu_{\mathrm{B}}/\mathrm{Mn}$. This is not a saturation value since the data show no sign of saturation when the temperature approaches 5 K.

At the end of these magnetization measurements the field was switched off and the remanent magnetization was measured while warming the film up to room temperature [Figs. 2(c)–2(d)]. The magnetic remanence data are exotic in two respects. Because $d_{\mathrm{nc}}^{\mathrm{lp}}$ is very short an antiferromagnetic order of the nanocolumns should occur through the nanocolumn dipolar coupling [14]. We thus expect no magnetic remanence at low temperature from the nanocolumns. The first surprise is the quite large remanent magnetic signal instead observed at 5 K, accounting for about 35% of the magnetic moment under 5 T. Moreover, it is nearly isotropic and almost disappears at 20 K [Fig. 2(d)] which is the position of the zero field cooling (ZFC) peak in low field magnetization measurements [Fig. 3(c)]. The second unexpected result is the magnetization uprise observed when warming the film from 20 K up to $\simeq 40$ K.

In order to understand these unexpected features a microscopic probe able to resolve the magnetic properties of the cores and shells is needed. It is provided by μSR spectroscopy.

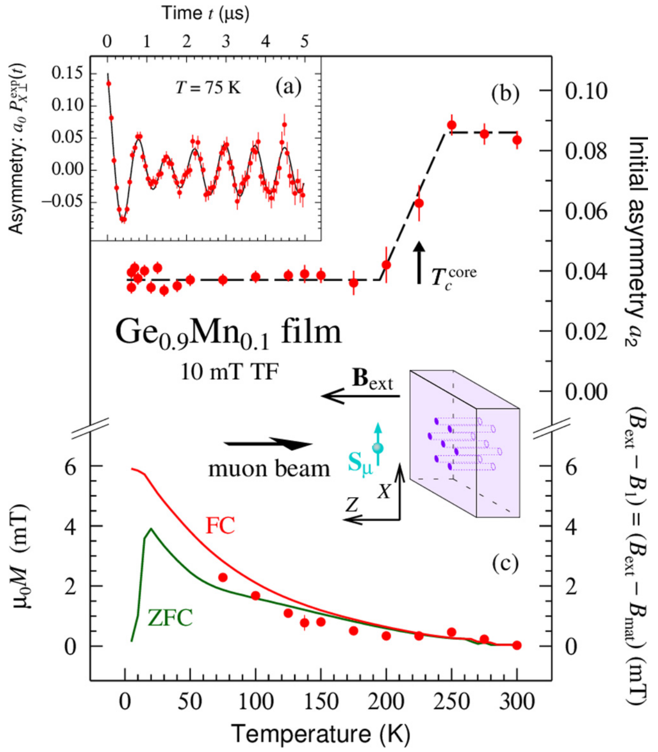

FIG. 3. (Color online) (a) A transverse-field (TF) μSR time spectrum recorded at 75 K and in a 10 mT field with the result of a fit to Eq. (1). (b) Thermal dependence of the asymmetry a_2, and (c) field difference $(B_{\mathrm{ext}} - B_1) = (B_{\mathrm{ext}} - B_{\mathrm{mat}})$ (bullets) compared to the field $\mu_0 M$, where M is the bulk magnetization (full lines) measured under $B_{\mathrm{ext}} = 10$ mT following either a field or zero-field cooling procedure. The TF-μSR geometry is illustrated with the pictogram. The dashed line in panel (b) is a guide to the eyes.

B. Muon spin rotation and relaxation

The technique consists in the implantation of fully polarized muons in the sample. Muons of low kinetic energy are used to ensure they are all stopped within the film thickness (Appendix C 1). The spin 1/2 of the muon precesses in the local field at the interstitial site it occupies. The local field is the sum of the field arising from the neighboring electronic magnetic moments and the external field if any [32]. A typical weak transverse-field (TF) μSR time spectrum $a_0 P_{X\perp}^{\mathrm{exp}}(t)$ recorded after a FC procedure is shown in Fig. 3(a). $P_{X\perp}^{\mathrm{exp}}(t)$ measures the evolution of the muon polarization along the X axis in a plane perpendicular to $\mathbf{B}_{\mathrm{ext}}$. As explained in Appendix C 2, for $40 \leqslant T \leqslant 300$ K the function

$$a_0 P_{X\perp}^{\mathrm{exp}}(t) = a_1 \exp[-(\lambda_{X\perp} t)^{\beta}] \cos(\gamma_\mu B_1 t + \varphi) + a_2 \cos(\gamma_\mu B_{\mathrm{ext}} t + \varphi) \tag{1}$$

provides a good fit to the data. Here φ is a phase constant, $a_1 = 0.13$, B_1 and a_2 are free parameters, and $\gamma_\mu = 851.6$ Mrad s^{-1} T^{-1} is the muon gyromagnetic ratio. The stretched exponential accounts for the magnetic inhomogeneity and dynamics of the first component. The exponent β has been set in consistency with zero-field (ZF) data. The relaxation rate $\lambda_{X\perp}$ is so large below 40 K that it cannot be determined with confidence. Still the second component can be analyzed after dropping the initial channels and setting $a_1 = 0$ in Eq. (1). The temperature dependencies of a_2 and the field difference $(B_{\mathrm{ext}} - B_1)$ are displayed in Figs. 3(b)–3(c).

The muons being implanted randomly in the film, and the matrix between the columns occupying a volume bigger than that of the columns, it is legitimate to set $a_1 = a_{\mathrm{mat}}$ where a_{mat}/a_0 is the fraction of muons implanted in the matrix. Naturally we denote $B_1 = B_{\mathrm{mat}}$ the field probed by these muons. From Fig. 3(c) the field difference $B_{\mathrm{mat}} - B_{\mathrm{ext}}$ is on the order of $-\mu_0 M$. The sign of this field can be understood as follows. In the absence of Mn atoms in the matrix, it is essentially the dipolar field produced by the nanocolumns which is antiparallel to the column moments. Therefore the field in the matrix is essentially equal to $B_{\mathrm{ext}} - \mu_0 M$. We speculate the slight reduction in absolute value of the measured field compared to $-\mu_0 M$ below 200 K [see Fig. 3(c)] to arise from the Mn moments in the shells which are slightly polarized antiparallel to the cores; see Sec. IV and the interpretation of the remanence data in state 4.

We now turn to $a_2(T)$ [Fig. 3(b)]. As the film is cooled below 250 K, a_2 starts to decrease and it reaches a plateau at ≈ 200 K: We conclude that the nanocolumns enter a magnetically ordered state with an average ordering temperature $T_c^{\mathrm{col}} = 225$ K and a transition width ≈ 50 K [33]. This relatively large width could be associated with some inhomogeneity in the Mn concentration along the columns or in their diameter as has been evidenced in atom probe tomography [29]. In a weak TF-μSR experiment, the muons probing a magnetically ordered region—here the columns cores as will be shown below—and its vicinity are rapidly depolarized [34] and do not contribute to the signal. Therefore, we attribute the second component below 200 K to muons implanted in the sample surroundings, i.e., the so-called background with $a_{\mathrm{bg}} \simeq 0.035$, a reasonable value considering the area of our sample. Above T_c^{col}, the amplitude $a_{\mathrm{c}} = a_2 - a_{\mathrm{bg}} \simeq 0.05$ is assigned to muons in the

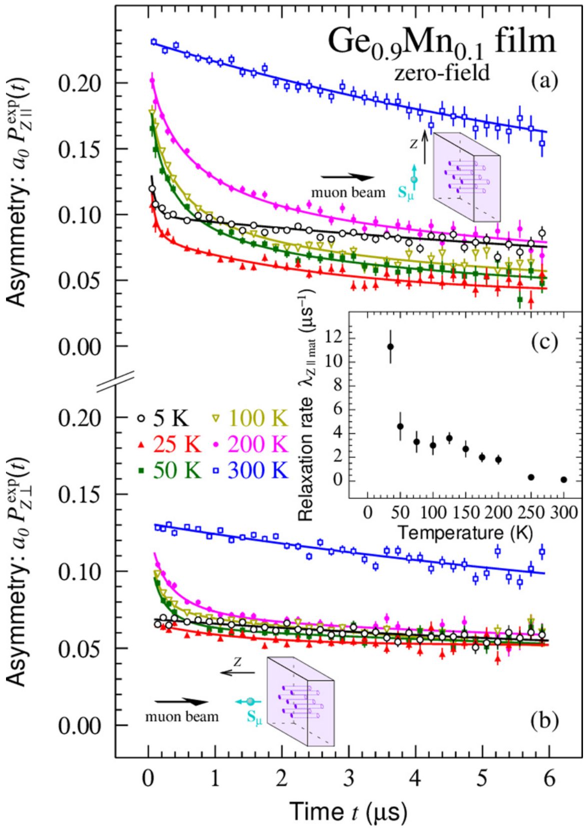

FIG. 4. (Color online) A selection of ZF-μSR time spectra for the $\mathrm{Ge_{0.9}Mn_{0.1}}$ film with $\mathbf{S}_\mu$ either parallel [panel (a)] or perpendicular [panel (b)] to the film substrate. The solid lines arise from fits. The thermal dependence of the μSR spin-lattice relaxation rate $\lambda_{Z\,\|\,\mathrm{mat}}$ is displayed in panel (c).

paramagnetic cores and their surroundings. The film volume fraction corresponding to the column cores and the region within a distance r from them is $\pi(d_{\mathrm{core}}/2+r)^2/[\sqrt{3}(d_{\mathrm{nc}}^{\mathrm{lp}})^2/2]$ which is equal to $a_{\mathrm{c}}/(a_{\mathrm{c}}+a_{\mathrm{mat}})$ provided that $r = 1.8$ nm. Such an r value is in the accepted range; see, e.g., Ref. [35].

The zero-field (ZF) μSR data provide a further insight into the magnetic moments of the columns and their dynamics. A selection of $a_0 P^{\mathrm{exp}}_{Z\,\|,\perp}(t)$ time spectra with the initial muon polarization $\mathbf{S}_\mu$ either parallel or perpendicular to the film substrate is shown in Fig. 4. $P^{\mathrm{exp}}_{Z\,\|,\perp}(t)$ denotes the evolution of the projection of the muon polarization along $\mathbf{S}_\mu$ which defines the Z axis. We note three qualitative characteristics. (i) The transition from the paramagnetic to the superparamagnetic states of the columns is fingerprinted by comparing the spectra at 300 and 200 K. (ii) Given the uniaxial character of the nanocolumns, the similitude of the spectra for the two geometries is striking. Since we probe the dynamics of the Mn spins, we conclude that we are dealing with spins with weak magnetocrystalline anisotropy, in agreement with Ref. [36]. (iii) With a column ordering temperature of $T_c^{\mathrm{col}} =$ 225 K, no magnetic excitation should be present at, say 25 K, i.e., $\approx T_c^{\mathrm{col}}/10$, in contradiction to the dynamical fields signalled by a nonzero slope of the spectra at long times. Given the core-shell structure of the columns, we assign these dynamical fields to the Mn ions in the shells and therefore the transition observed at 225 K by TF-μSR to the Mn ions in the cores, and consequently we denote $T_c^{\mathrm{col}} \equiv T_c^{\mathrm{core}}$.

A quantitative analysis of the dynamics probed by the ZF-μSR measurements is given in Appendix C 3. The muon spin-lattice relaxation rate $\lambda_{Z\,\|\,\mathrm{mat}}$ deduced from this analysis is proportional to the fluctuation time τ of the Mn spins in the shells. A sharp increase of τ is inferred below 50 K [Fig. 4(c)], indicating the onset of a fluctuation slowing down. This is consistent with the general picture that we propose below for the magnetic properties of the nanocolumns, in particular the onset of a magnetization signal from the shells below $\approx$30 K [Fig. 2(a)] and the drop of the shell signal at $\approx$20 K in the remanence data [Fig. 2(d)]. ZF-μSR and SQUID measurements probe the spin freezing at different temperatures because of their different time scales, on the order of a nanosecond for the former [32] and of a minute for the latter.

IV. CORE-SHELL MAGNETIC NANOSTRUCTURE

We now provide a picture for the magnetic behavior of the nanocolumns. It is illustrated in Fig. 5 for the different characteristic regimes found in the magnetization and remanence data and labeled by numbers 1 through 5 in Fig. 2. It is based on the fact that the core-shell splitting found in the microstructure also pertains to the magnetic properties as indicated by the ZF-μSR experiment. In addition our picture implies that there is no exchange coupling between the core and the shell and that the magnetic behavior of the shell is spin-glass-like. These two hypotheses will be subsequently discussed.

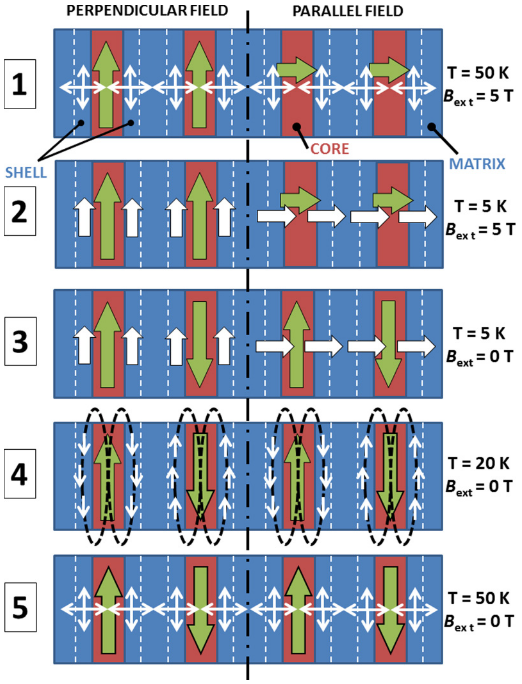

FIG. 5. (Color online) Schematic magnetic configurations for the cores and shells for fields and temperatures defined as labels in Fig. 2. The $\mathbf{B}_{\mathrm{ext}}$ direction is relative to the film substrate. The green arrows refer to the magnetic moment of the cores. Wide white arrows refer to the polarized frozen spin-glass-like state in the shells, while narrow arrows sketch a paramagnetic state. The curly dashed lines in panel 4 sketch the dipolar field from the cores.

We assign the signal in state 1 to the magnetic moments of the cores which are aligned parallel to $\mathbf{B}_{\mathrm{ext}}$. Considering their nanometer size, the nanocolumns behave as superparamagnetic nanostructures in SQUID measurements. Their maximum blocking temperature is $T_{\mathrm{B}}^{\mathrm{SQUID}} = 150$ K given by the vanishing remanence in Fig. 2(c) and the bifurcation between ZFC and FC curves in Fig. 3(c). In state 1 the shells are paramagnetic and essentially they do not contribute to the signal. When the temperature is lowered to 5 K (state 2) the Mn moments in the shells freeze. Because of the spin-glass-like state, both ferro- and antiferromagnetic couplings should be present between the Mn moments. The resulting magnetization is aligned parallel to $\mathbf{B}_{\mathrm{ext}}$, and the average value of 0.6 $\mu_{\mathrm{B}}/\mathrm{Mn}$ deduced from Figs. 2(a)–2(c) should therefore not be regarded as the intrinsic value for Mn moments. A field much larger than 5 T is certainly required to ferromagnetically align them. State 3 is obtained after cancellation of $\mathbf{B}_{\mathrm{ext}}$. In the case where this field was parallel to the film, the core magnetization spontaneously aligns along the column axes owing to their shape anisotropy since the column cores are 80 nm long and their diameter is 2 nm. Now, it becomes energetically favorable for neighboring cores to align antiparallel under the mutual influence of their dipolar fields. The lattice formed by the columns being triangular, this situation leads to strong frustration. The Mn magnetic moments in the shells which are not magnetically coupled to the cores are unaffected by their rearrangement. This is testified by the same value found for the shell magnetization in Figs. 2(a) and 2(c), i.e., in the magnetization and remanence data. Upon warming up to 20 K (state 4), dynamics sets in on the time scale of the SQUID measurements among the Mn moments in the shells: Their contribution to the magnetization rapidly drops. In fact, as revealed by the upturn of the signal above 20 K, the shell Mn moments are slightly polarized antiparallel to their core due to its stray field. For $\mathbf{B}_{\mathrm{ext}}$ perpendicular to the film substrate, a sizable remanent signal is detected at 20 K and above. We attribute it to imperfections in the nanocolumn array (see Appendix B) which inhibit a perfect cancellation of the core moments. Upon further warming the polarization of the shells by the core is less effective: The global magnetization of the film goes through a local maximum before the effect of superparamagnetism in the column cores takes over (state 5), and the film remanent magnetization ultimately vanishes at $\simeq$150 K.

The absence of magnetic coupling between the Mn magnetic moments in the cores and shells is traced back to the strains present at the interface, the signature of which is the dark ring in Fig. 1(b). The large difference between the crystal lattice of the core (metallic phase of alpha-type $\mathrm{Ge_2Mn}$) and shell (more diamondlike) prevents any epitaxial relationship at their interface and thus any atomic continuity [28]. This leads to the formation of interface dangling bonds and dislocations breaking the magnetic coupling between the core and shell. The shell structure is highly disordered owing to the strong Mn concentration gradient. This gives rise to random interactions and magnetic frustration favoring a spin-glass-like state. The core-shell magnetic separation could probably be observed in other transition metal doped semiconductors grown at moderate temperature like GaMnAs [37], GaFeN [9], GeFe [38], and ZnCrTe [8].

V. CONCLUSIONS

The $\mathrm{Ge_{0.9}Mn_{0.1}}$ film of self-organized nanocolumns is a complex object. The columns comprise a core of diameter 2 nm with a Mn atomic concentration of $\approx$65% and a shell of thickness 1 nm in which the Mn concentration decreases to 0. The Mn concentration in the matrix between the columns is below the detection limit of 0.05%. A transition from a paramagnetic to a superparamagnetic state is observed for the cores around 225 K. Below 150 K they become progressively blocked on the SQUID time scale. No magnetic order is found for the magnetic moments in the shells. Their spin dynamics is rather isotropic. The shell magnetic moments start to slow down on the nanosecond time scale below 50 K. There is no magnetic coupling between a column core and its shell, except for a weak dipolar coupling. Finally we suggest that the separation in three distinct structural and magnetic regions observed here is generic to semiconductors doped with a nonmiscible transition element.

ACKNOWLEDGMENTS

The authors acknowledge the support of the French Agence Nationale de la Recherche (ANR), under Grant No. ANR-13-BS10-0002 (project SiGeSPIN). Part of this work has been performed at the Swiss Muon Source (SμS), Paul Scherrer Institute, Villigen, Switzerland. We thank J.-F. Jacquot for his help during the SQUID measurements.

APPENDIX A: TRANSMISSION ELECTRON MICROSCOPY AND ELECTRON ENERGY LOSS SPECTROMETRY CHARACTERIZATION

Transmission electron microscopy (TEM) measurements were performed using a monochromated and double-corrected 80–300 kV FEI Titan^3 Ultimate microscope working at 200 kV. Taking advantage of the image-side aberration corrector, high resolution TEM (HRTEM) images were acquired close to Gaussian focus, i.e., within a few nanometers away

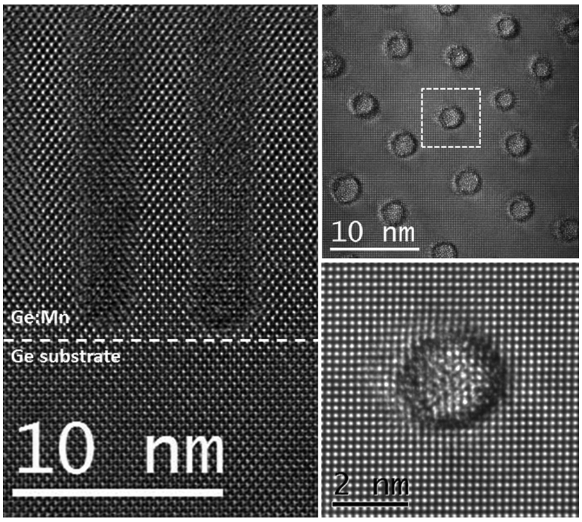

FIG. 6. Low and high resolution TEM images of the $\mathrm{Ge_{0.9}Mn_{0.1}}$ film: cut (left) and top views (right).

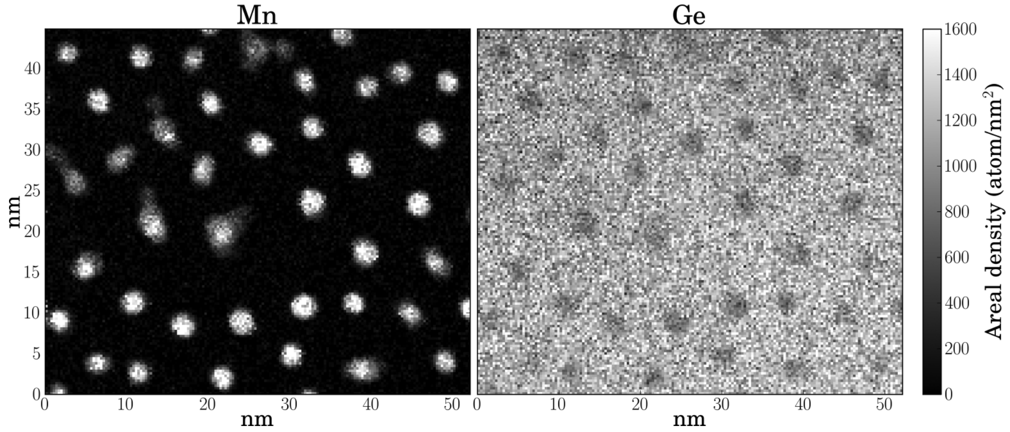

FIG. 7. Mn and Ge areal density maps obtained by EELS measurements.

to avoid delocalization effect. To increase the signal-to-noise ratio of the HRTEM measurement, a series of about 10 images has been acquired from the same area. After alignment of the image series using a cross-correlation based algorithm, we averaged the images over the series, to obtain an HRTEM image with very good signal-to-noise ratio. TEM images of a $Ge_{0.9}Mn_{0.1}$ film grown at 100 °C are shown in Fig. 6.

Electron energy loss spectroscopy (EELS) acquisitions were achieved using a Gatan imaging filter (GIF) Quantum in dual-EELS mode with an energy dispersion of 1 eV, allowing us to acquire a full range electron energy loss from 0 to 1400 eV. The convergence and collection angles were 20 and 98 mrad, respectively. Typical pixel acquisition time was 20–50 ms and the typical map size was about 200 × 200 pixels. The pixel size was set to 0.3 nm. The noise of the EELS signal was removed using a principal component analysis (PCA) algorithm implemented in the open-source software Hyperpsy [39]. The relevant number of components for the reconstruction of the spectra was chosen by careful inspection of the factors and loadings of the first 10 components. For each edge (Mn $L_{2,3}$ at 640 eV and Ge $L_{2,3}$ at 1217 eV), the background was removed by subtracting a power law fitted in the region preceding the edge with a width of 40–80 eV (depending on the edge). Element maps were obtained by integrating over 60 eV after the edge for Mn and Ge.

Theoretically, the signal of ionization edge I_k can be quantified using the standardless method, following the relation:

$$I_k = n_{\mathrm{den}} I \sigma_k \tag{A1}$$

where n_{den} is the areal density (atom/nm^2) of a given element, I is the total integrated number of counts in the spectrum, and σ_k is the cross section of ionization of an electron in the corresponding electron shell. Taking advantage of the high dynamical range of the spectra provided by the acquisition in dual-EELS mode, we can measure the total integrated number of counts I [Eq. (A1)] in the spectrum—from the intense zero-loss peak to the Ge and Mn edges.

In practice, the integration is performed over an energy range Δ, and the collection angle β is limited by the entrance aperture of the spectrometer. These experimental parameters are taken into account in the calculation of the partial cross sections, which depend on Δ, on the collection angle β, and on the energy loss. For the Ge and Mn quantification we calculated parameterized partial Hartree-Slater cross sections [40] using the Gatan Digital Micrograph software. By further measuring the specimen thickness, we can calculate the absolute volumic density (atom/nm^3) of each species.

To check the reliability of our analysis, we performed two cross checks:

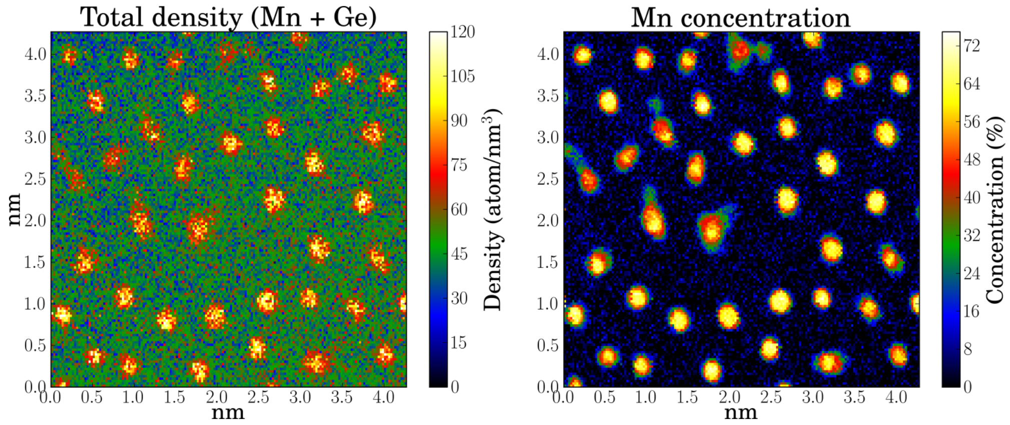

FIG. 8. (Color online) Total density and Mn relative concentration maps obtained by EELS measurements.

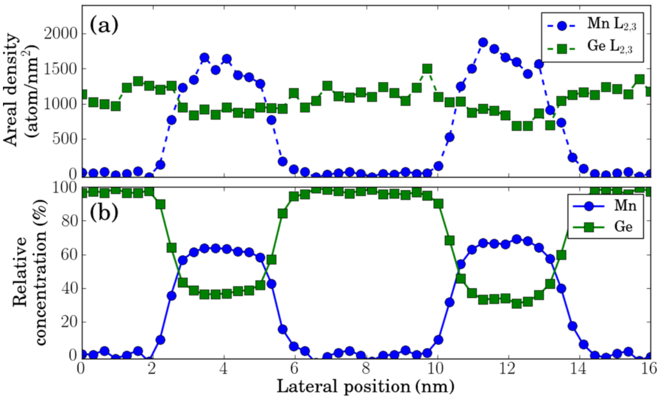

FIG. 9. (Color online) (a) Areal density and (b) relative concentration profiles measured across two nanocolumns.

(1) The experimental value for the Ge volumic density in the diamond Ge pure matrix is in good agreement—within 10%—with the corresponding theoretical value (44 atoms/nm^3).

(2) The Mn concentration averaged over the whole concentration map is in good agreement—within 2%—with the Mn nominal concentration of the film measured with Rutherford backscattering spectrometry (RBS).

Figure 7 shows the Mn and Ge areal density maps obtained by the method explained previously. The total density (Mn + Ge density) is calculated by dividing the total areal density (Mn + Ge areal density) by the specimen thickness. Figure 8 shows the total density and the Mn relative concentration maps. Profiles measured on two nanocolumns are plotted in Fig. 9.

APPENDIX B: ESTIMATE OF THE NANOCOLUMN LATTICE CORRELATION LENGTH

The nanocolumns form a triangular lattice with a lattice parameter $d_{\rm nc}^{\rm lp} = 10$ nm. Here we provide an estimate for the correlation length of the lattice using fast Fourier transforms (FFT) of the TEM images. Figure 10 shows examples. While peaks are visible on the FFT of a small fraction (20×20 nm^2) of the TEM image, only a ring is seen when a larger area (60×60 nm^2) of the original image is considered. For an even larger area (not shown) no structure appears on the FFT. We therefore conclude that the correlation length of the nanocolumn lattice is a few tens of nanometers, i.e., a few lattice parameters.

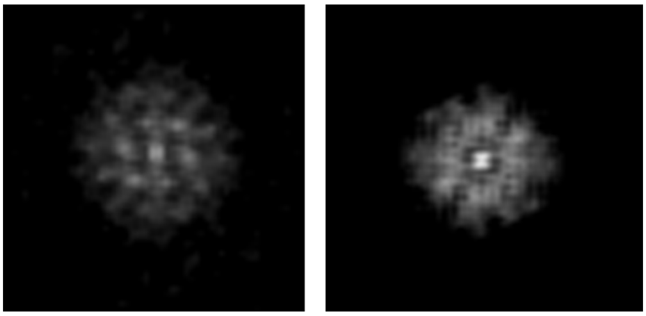

FIG. 10. Typical fast Fourier transforms of 20×20 nm^2 (left) and 60×60 nm^2 (right) portions of a TEM image.

APPENDIX C: MUON SPIN ROTATION AND RELAXATION MEASUREMENTS

In this Appendix we first display the muon implantation profile computed for muons of 7.5 keV kinetic energy. In the subsequent section we provide additional information on the TF-μSR measurements. We finally describe the detailed analysis of the ZF-μSR data.

1. Muon implantation profile

Muons of 7.5 keV kinetic energy were used for the μSR measurements. From the implantation depth profile shown in Fig. 11, we can conclude that all the muons are implanted within the film thickness of 80 nm.

2. Transverse field μSR

The TF-μSR time spectrum displayed in Fig. 3(a) exhibits two beating oscillating components. A first analysis for $100 \leqslant T \leqslant 200$ K indicates the amplitude of the more rapidly damped component to be temperature independent. Below 100 K the damping of this first component becomes quite large. As a consequence its initial amplitude, damping rate, precession frequency, and initial phase are determined with limited precision. Fixing the initial amplitude allows a better accuracy on the other three parameters down to 40 K. To a good approximation, the precession frequency of the second component is constant in the whole temperature range with an average value $\nu_2 = 1.353$ MHz. This corresponds to $B_{\rm ext}$, i.e., $\nu_2 = \nu_{\rm ext} = \gamma_\mu B_{\rm ext}/(2\pi)$. This discussion justifies the use of Eq. (1) for the analysis of the TF-μSR time spectra.

3. Zero field μSR

From the two time spectra recorded at 300 K, see Fig. 4 of the main text, we measure $a_0 \simeq 0.23$ (0.13) when $\mathbf{S}_\mu$ is parallel (perpendicular) to the film substrate. The smaller a_0 value for the perpendicular geometry follows from the geometrical setup of the spectrometer.

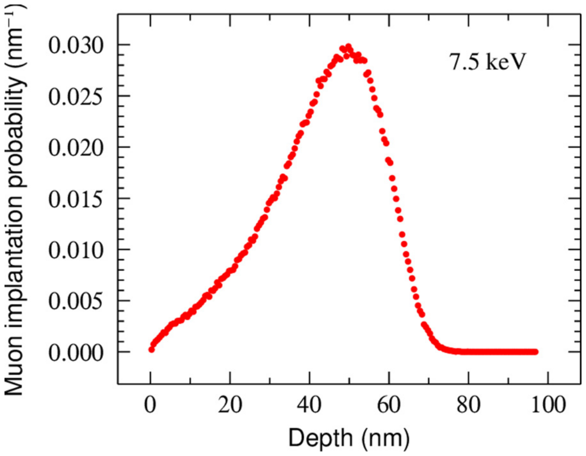

FIG. 11. (Color online) Distribution of the depth implantation profile for muons of 7.5 keV kinetic energy. The simulation has been performed using the Monte Carlo TRIM.SP code [26,41,42] for a GeMn film with a Ge:Mn atomic ratio of 9:1.

A qualitative discussion of the ZF spectra is given in the main text. Here we quantitatively describe them. The measured asymmetry can be modeled consistently with the TF-μSR model

$$a_0 P_{Z\parallel}^{\rm exp}(t) = \alpha\{a_{\rm mat}\exp[-(\lambda_{Z\parallel{\rm mat}}t)^{\beta}] + a_{\rm c}'\exp(-\lambda_{Z\parallel{\rm c}}t) + a_{\rm bg}\}, \quad \text{(C1)}$$

where $\lambda_{Z\parallel{\rm mat}}$ and $\lambda_{Z\parallel{\rm c}}$ are spin-lattice relaxation rates. Given the similitude of the data recorded for the initial muon polarization perpendicular and parallel to the film and since a_0 is much larger for the latter geometry, we concentrate our discussion on it. The $\alpha = 1.05$ geometrical parameter in Eq. (C1) is introduced to account for the slight difference in the signal amplitude between the TF and ZF geometries. Naturally we assign the first (second) term in Eq. (C1) to muons stopped in the matrix (cores and their vicinity), while the last one concerns muons which have missed the sample. We find values for $a_{\rm mat}$ and $a_{\rm bg}$ in line with the TF results. The weight of the second component is $a_{\rm c}' \simeq 0.05$ in the whole temperature range: Contrary to the transverse field case, the signal associated with the muons stopped in the cores and their vicinity is not lost below $T_c^{\rm core}$. Fitting Eq. (C1) to the data, we obtain $\lambda_{Z\parallel{\rm mat}}(T)$ [Fig. 4(c)] and an exponent β equal to 0.6 between 200 and 50 K with a tendency to increase at lower temperature. At room temperature, $\beta = 1$ provides a good fit to the data. The relaxation rate $\lambda_{Z\parallel{\rm c}}$ is relatively small ($\lambda_{Z\parallel{\rm c}} \lesssim 0.3\ \mu{\rm s}^{-1}$) but not zero in the whole temperature range.

Recalling the results obtained in TF measurements, and the structure of the film, we deduce that the distance from muons concerned by the first component in Eq. (C1) to the nearest Mn ions spans between 0.8 and $\simeq$3.8 nm [43]. This is a situation reminiscent of the dilute canonical spin glasses. In such systems, the polarization function has been derived in the case of fast fluctuating moments to be $P_Z(t) = \exp[-\sqrt{\lambda_Z t}]$ [32,44], a function which is close to our observation. The relaxation rate λ_Z is related to the magnetic fluctuation time τ of the Mn spins in the shell through the formula $\lambda_Z = 4\gamma_\mu^2\Delta_{\rm L}^2\tau$, where $\Delta_{\rm L}$ is the half width at half maximum of the component field Lorentzian distribution [45].

We have simulated the distribution of the Cartesian field components in the film region probed by muons associated with the first component in Eq. (C1) above or in Eq. (1). This is the part of the matrix located at a minimum distance of $d_{\rm c}/2 + r = 2.8$ nm from any nanocolumn center. For the simulation we locate the columns on the nodes of a triangular lattice. The core magnetization (827 kA/m) is set along the direction of the column with a random orientation parallel or antiparallel to it. For the shells, we consider atomic magnetic moments of $0.6\mu_{\rm B}$ with random orientation and a density linearly decreasing from 57 atoms/nm^3 at 1 nm from the nanocolumn center to 0 atoms/nm^3 at 2 nm from it. After a depth average according to the muon implantation profile of Fig. 11, the distributions for the two field components perpendicular to the nanocolumns are found to be fairly approximated by a Lorentzian function of about 0.5 mT half width at half maximum (HWHM). The field component parallel to the columns is nearly Gaussian with 2.3 mT HWHM. While the Lorentzian line shape for the distribution of the first two components is consistent with the observed stretched exponential function $\exp[-(\lambda_{Z\parallel{\rm mat}}t)^{\beta}]$, the case for the third component is not so clear. Interestingly, if one takes a muon implantation profile uniform along the film depth, the distribution of the third component approaches a Lorentzian function and the anisotropy with the first two components which remain Lorentzian is reduced. Since the influence of the top and bottom surfaces of the film is reinforced in this second simulation, our result suggests that the muon response may be influenced by nanocolumns which would not extend over the whole film thickness. Other effects not accounted for in our simulations, such as (i) the existence of correlations in the orientations of the cores magnetization in the frustrated triangular lattice they form or (ii) the finite coherence length for this triangular lattice may also play a role. The study of these effects is out of the scope of this report.

Finally a few ZF spectra have been recorded after prior cooling of the film with $B_{\rm ext} = 150$ mT perpendicular to the film substrate. Within the data error bars no difference is found with the spectra measured after the usual ZFC procedure.

[1] I. Žutić, J. Fabian, and S. Das Sarma, Rev. Mod. Phys. **76**, 323 (2004).

[2] A. H. MacDonald, P. Schiffer, and N. Samarth, Nat. Mater. **4**, 195 (2005).

[3] T. Dietl, Nat. Mater. **9**, 965 (2010).

[4] H. Ohno, Nat. Mater. **9**, 952 (2010).

[5] C. Timm, J. Phys.: Condens. Matter **15**, R1865 (2003).

[6] T. Dietl, K. Sato, T. Fukushima, A. Bonanni, M. Jamet, A. Barski, S. Kuroda, M. Tanaka, Pham Nam Hai, and H. Katayama-Yoshida, arXiv:1412.8062 [Rev. Mod. Phys. (to be published)].

[7] D. Bougeard, S. Ahlers, A. Trampert, N. Sircar, and G. Abstreiter, Phys. Rev. Lett. **97**, 237202 (2006).

[8] S. Kuroda, N. Nishizawa, K. Takita, M. Mitome, Y. Bando, K. Osuch, and T. Dietl, Nat. Mater. **6**, 440 (2007).

[9] A. Bonanni, A. Navarro-Quezada, T. Li, M. Wegscheider, Z. Matěj, V. Holý, R. T. Lechner, G. Bauer, M. Rovezzi, F. D'Acapito, M. Kiecana, M. Sawicki, and T. Dietl, Phys. Rev. Lett. **101**, 135502 (2008).

[10] T.-G. Le, D. N. H. Nam, M. T. Dau, T. K. P. Luong, N. V. Khiem, V. L. Thanh, L. Michez, and J. Derrien, J. Phys.: Conf. Ser. **292**, 012012 (2011).

[11] A. P. Li, C. Zeng, K. van Benthem, M. F. Chisholm, J. Shen, S. V. S. Nageswara Rao, S. K. Dixit, L. C. Feldman, A. G. Petukhov, M. Foygel, and H. H. Weitering, Phys. Rev. B **75**, 201201 (2007).

[12] D. Bougeard, N. Sircar, S. Ahlers, V. Lang, G. Abstreiter, A. Trampert, J. M. LeBeau, S. Stemmer, D. W. Saxey, and A. Cerezo, Nano Lett. **9**, 3743 (2009).

[13] Y. Wang, F. Xiu, Y. Wang, X. Kou, A. P. Jacob, K. L. Wang, and J. Zou, J. Alloys Compd. **508**, 273 (2010).

[14] M. Jamet, A. Barski, T. Devillers, V. Poydenot, R. Dujardin, P. Bayle-Guillemaud, J. Rothman, E. Bellet-Amalric, A. Marty, J. Cibert, R. Mattana, and S. Tatarenko, Nat. Mater. **5**, 653 (2006).

[15] Y. Nishio, K. Ishikawa, S. Kuroda, M. Mitome, and Y. Bando, MRS Proc. **1183**, 1183-FF01-11 (2009).

[16] S. Ahlers, P. R. Stone, N. Sircar, E. Arenholz, O. D. Dubon, and D. Bougeard, Appl. Phys. Lett. **95**, 151911 (2009).

[17] S. Tardif, S. Cherifi, M. Jamet, T. Devillers, A. Barski, D. Schmitz, N. Darowski, P. Thakur, J. Cezar, N. Brookes, R. Mattana, and J. Cibert, Appl. Phys. Lett. **97**, 062501 (2010).

[18] S. Tardif, A. Titov, E. Arras, I. Slipukhina, E.-K. Hlil, S. Cherifi, Y. Joly, M. Jamet, A. Barski, J. Cibert, E. Kulatov, Y. A. Uspenskii, and P. Pochet, J. Magn. Magn. Mater. **354**, 151 (2014).

[19] R. Morgunov, M. Farle, M. Passacantando, L. Ottaviano, and O. Kazakova, Phys. Rev. B **78**, 045206 (2008).

[20] A. Jain, M. Jamet, A. Barski, T. Devillers, C. Porret, P. Bayle-Guillemaud, S. Gambarelli, V. Maurel, and G. Desfonds, Appl. Phys. Lett. **97**, 202502 (2010).

[21] A. Jain, M. Jamet, A. Barski, T. Devillers, I.-S. Yu, C. Porret, P. Bayle-Guillemaud, V. Favre-Nicolin, S. Gambarelli, V. Maurel, G. Desfonds, J. F. Jacquot, and S. Tardif, J. Appl. Phys. **109**, 013911 (2011).

[22] T. Devillers, M. Jamet, A. Barski, V. Poydenot, P. Bayle-Guillemaud, E. Bellet-Amalric, S. Cherifi, and J. Cibert, Phys. Rev. B **76**, 205306 (2007).

[23] I.-S. Yu, M. Jamet, T. Devillers, A. Barski, P. Bayle-Guillemaud, C. Beigné, J. Rothman, V. Baltz, and J. Cibert, Phys. Rev. B **82**, 035308 (2010).

[24] M. M. Özer, J. R. Thompson, and H. H. Weitering, Phys. Rev. B **85**, 125208 (2012).

[25] T. Fukushima, K. Sato, H. Katayama-Yoshida, and P. Dederichs, Jpn. J. Appl. Phys., Part 2 **45**, L416 (2006).

[26] E. Morenzoni, T. Prokscha, A. Suter, H. Luetkens, and R. Khasanov, J. Phys.: Condens. Matter **16**, S4583 (2004).

[27] T. Prokscha, E. Morenzoni, K. Deiters, F. Foroughi, D. George, R. Kobler, A. Suter, and V. Vrankovic, Nucl. Instr. Meth. A **595**, 317 (2008).

[28] E. Arras, F. Lançon, I. Slipukhina, E. Prestat, M. Rovezzi, S. Tardif, A. Titov, P. Bayle-Guillemaud, F. d'Acapito, A. Barski, V. Favre-Nicolin, M. Jamet, J. Cibert, and P. Pochet, Phys. Rev. B **85**, 115204 (2012).

[29] I. Mouton, R. Lardé, E. Talbot, E. Cadel, C. Genevois, D. Blavette, V. Baltz, E. Prestat, P. Bayle-Guillemaud, A. Barski, and M. Jamet, J. Appl. Phys. **112**, 113918 (2012).

[30] M. Rovezzi, T. Devillers, E. Arras, F. D'Acapito, A. Barski, M. Jamet, and P. Pochet, Appl. Phys. Lett. **92**, 242510 (2008).

[31] S. Tardif, V. Favre-Nicolin, F. Lançon, E. Arras, M. Jamet, A. Barski, C. Porret, P. Bayle-Guillemaud, P. Pochet, T. Devillers, and M. Rovezzi, Phys. Rev. B **82**, 104101 (2010).

[32] A. Yaouanc and P. Dalmas de Réotier, *Muon Spin Rotation, Relaxation, and Resonance: Applications to Condensed Matter*, International Series of Monographs on Physics Vol. 147 (Oxford University Press, Oxford, 2011).

[33] One could conceive the transition from the paramagnetic to superparamagnetic states of the column cores to take place above room temperature and that the blocking temperature corresponding to the TF-μSR technique is around 225 K where $a_2(T)$ drops, while it is around $T_{\mathrm{B}}^{\mathrm{SQUID}} = 150$ K for the SQUID measurements (see Sec. IV for the definition of $T_{\mathrm{B}}^{\mathrm{SQUID}}$). Recalling that the characteristic time scale of TF-μSR is $(\gamma_\mu B_{\mathrm{ext}})^{-1} \simeq 0.1$ μs in our case, this interpretation of the data would lead to an unrealistic short attempt time and therefore cannot hold.

[34] G. M. Luke, A. Keren, K. Kojima, L. P. Le, B. J. Sternlieb, W. D. Wu, Y. J. Uemura, Y. Ōnuki, and T. Komatsubara, Phys. Rev. Lett. **73**, 1853 (1994).

[35] C. Niedermayer, C. Bernhard, T. Blasius, A. Golnik, A. Moodenbaugh, and J. I. Budnick, Phys. Rev. Lett. **80**, 3843 (1998).

[36] A. Continenza, G. Profeta, and S. Picozzi, Phys. Rev. B **73**, 035212 (2006).

[37] J. Sadowski, J. Z. Domagala, R. Mathieu, A. Kovacs, and P. Dłużewski, J. Phys.: Condens. Matter **25**, 196005 (2013).

[38] Y. Shuto, M. Tanaka, and S. Sugahara, Appl. Phys. Lett. **90**, 132512 (2007).

[39] Hyperspectral data analysis toolbox, see http://hyperspy.org/.

[40] R. Egerton, *Electron Energy-Loss Spectroscopy in the Electron Microscope*, 3rd ed. (Springer, New York, Dordrecht, Heidelberg, London, 2011).

[41] W. Eckstein, *Computer Simulation of Ion-Solid Interactions* (Springer, Berlin, 1991).

[42] E. Morenzoni, H. Glückler, T. Prokscha, R. Khasanov, H. Luetkens, M. Birke, E. Forgan, C. Niedermayer, and M. Pleines, Nucl. Instr. Meth. B **192**, 254 (2002).

[43] The shorter distance is $d_{\mathrm{core}}/2 + r - (d_{\mathrm{core}}/2 + r_{\mathrm{s}}) = 0.8$ nm, with parameters defined in the main text. The larger distance is computed assuming the muon to be at the center of an equilateral triangle of side $d_{\mathrm{nc}}^{\mathrm{lp}}$.

[44] Y. J. Uemura, T. Yamazaki, D. R. Harshman, M. Senba, and E. J. Ansaldo, Phys. Rev. B **31**, 546 (1985).

[45] R. E. Walstedt and L. R. Walker, Phys. Rev. B **9**, 4857 (1974).